Theory of valence-band Auger line shapes: Ideal Si (111), (100), and (110)*

Peter J. Feibelman and E. J. McGuire
Sandia Laboratories, Albuquerque, New Mexico 87115

K. C. Pandey
IBM Watson Research Center, Yorktown Heights, New York 10598

(Received 23 August 1976; revised manuscript received 28 December 1976)

We report independent-electron model calculations of the $L_{2,3}VV$ and $L_1L_{2,3}V$ Auger line shapes for ideal Si (111), (100), and (110) surfaces and compare the results to data of Houston, Lagally, and Moore. For the $L_{2,3}VV$ transitions, agreement between experiment and theory is excellent, in contrast to poor agreement between experiment and the self-fold of the occupied Si density of states; this result shows that matrix-element angular momentum dependence and not many-electron effects cause the latter discrepancy. For the $L_1L_{2,3}V$ lines our calculated results are less satisfactory. We suggest that the disagreement between theory and data for these "Coster-Kronig" transitions is due to the difficulty of calculating accurate Auger matrix elements at low energies and, perhaps, to the use of "ideal" (i.e., unreconstructed) surface geometries in modeling actual Si surfaces.

I. INTRODUCTION

Measured valence-band Auger line shapes rarely, if ever, agree with the predictions of the corresponding density-of-states (DOS) models,[1] or in other words, with the line shapes obtained under the assumptions: (a) that the independent-particle picture is valid; and (b) that Auger matrix element variation is negligible across the valence band. An example of such a disagreement is shown in Figs. 1 and 2, in which the $L_{2,3}VV$ (i.e., $2p$–valence-band–valence-band) Auger line shapes for Si(111) and Si(100) surfaces, measured by Houston, Lagally, and Moore[2] are compared to the corresponding weighted self-folds of the occupied density of states (WSFDOS's[3]) of Si. The purpose of the work presented in this paper is to determine, for the specific case of Si, which of assumptions (a) and (b) is the source of the disagreement. Since a direct test of assumption (a) would entail the development of a many-electron theory of Auger spectroscopy, it seems more reasonable to investigate assumption (b) first. Thus we present below the first complete independent-particle calculations of valence-band Auger line shapes for a solid, Si.[4] Our calculations are "complete," of course, in that matrix elements have specifically been retained.

We report and discuss our results in Sec. IV of this paper. Our main conclusion is that, at least for the $L_{2,3}VV$ lines of Si, good agreement with measured Auger line shapes can be obtained within an independent-particle calculation, if matrix element variation across the valence band is not ignored. The important matrix element variation for Si occurs as a function of the angular momentum of the valence electrons which participate in the Auger process. Since the angular momentum character of the Si valence band changes from s-like near the band minimum to p-like near the maximum, the rather strong angular momentum dependence of the Auger matrix elements is equivalent to a strong effective energy dependence. It is this effective energy dependence which largely explains the difference between the DOS model

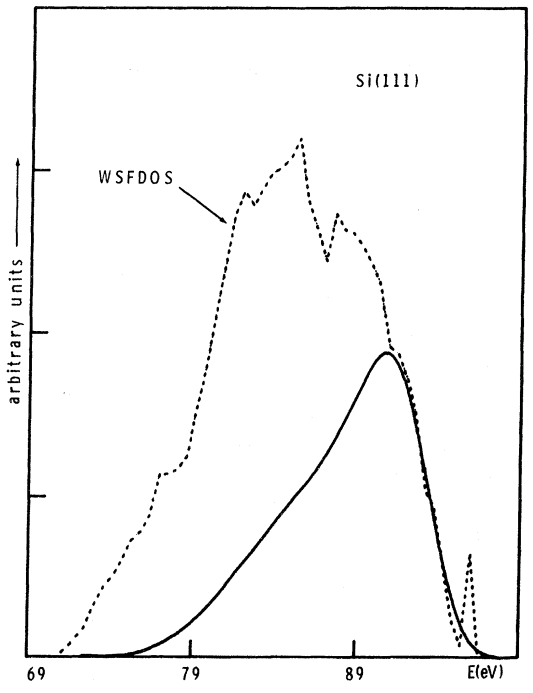

FIG. 1. Comparison of $L_{2,3}VV$ Auger line shape for Si(111) (solid line) measured by Houston, Lagally, and Moore (Ref. 2) with the weighted self-fold of the Si(111) density of states (defined in Ref. 3), with $\lambda = 7$ Å.

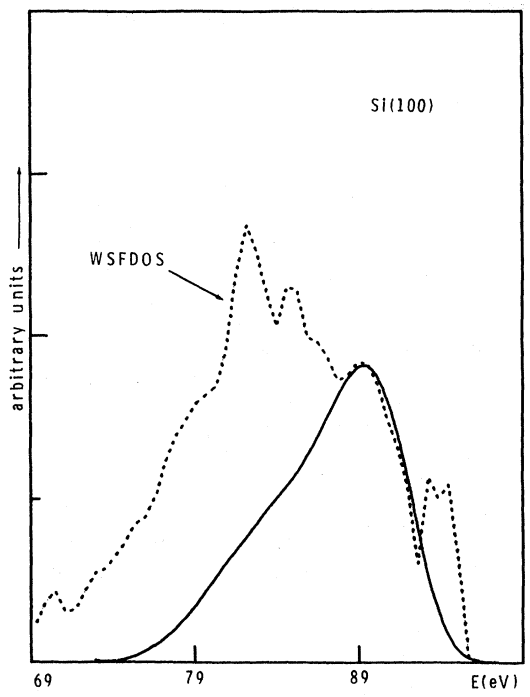

FIG. 2. Comparison of $L_{2,3}VV$ Auger line shape for Si(100) (solid line), of Ref. 2, compared with the WSFDOS of Si(100) (dashed line), with $\lambda = 7$ Å.

and experimental line shapes shown in Figs. 1 and 2.

We report results below not only for the $L_{2,3}VV$ Auger lines but also for the $L_1L_{2,3}V$ "Coster-Kronig" transitions on the Si (111), (100), and (110) surfaces. Predicting the $L_1L_{2,3}V$ line shapes is at the outset expected to provide a considerably more stringent test of the theory than predicting those of the $L_{2,3}VV$ transitions, for two reasons:

(i) The $L_1L_{2,3}V$ lines of Si lie at only ~ 35 eV (as against ~ 85 eV for the $L_{2,3}VV$ lines). Thus the $L_1L_{2,3}V$ Auger matrix elements are more difficult to calculate accurately.

(ii) Since the $L_1L_{2,3}V$ transitions involve only one valence electron, the $L_1L_{2,3}V$ data are to be compared not to a self-fold of the DOS but to the DOS itself (weighted by matrix elements, of course). But self-folding a DOS generally causes whatever structure it showed to become weaker and broader. Thus we expect sharper, more prominent features to appear in the $L_1L_{2,3}V$ line shapes than in the $L_{2,3}VV$, and we may anticipate the need for accurate surface geometric models to explain such features.

Both of these problems do turn out to affect our comparison of theory and experiment for the $L_1L_{2,3}V$ transitions. Although we find reasonable agreement between the positions of the principal structures in the $L_1L_{2,3}V$ data and "bulk" structures in the corresponding theoretical results, there are numerous "surface" structures in the theory which are absent in the data. At the same time, the theoretical results suggest that the lower-energy (s-like) part of the valence band should be more prominent in the line shapes, while the reverse turns out to be true.

We suggest, below (Sec. IV), that the absence of the surface structures in the $L_1L_{2,3}V$ data may be due to our use of "ideal" surface models to represent actual reconstructed Si surfaces. For appropriate surface models, that is, we believe that there might no longer be any predicted surface structures in the line shapes. We also suggest that the prediction of line shapes weighted more heavily on the lower-energy side is due to inaccuracy of the atomic matrix elements used in our tight-binding calculation. On the other hand the real source of the discrepancies between the $L_1L_{2,3}V$ data and theory may be many-electron effects of some sort which, e.g., broaden the surface features of the one-electron theory out of existence. At present this is an open question.

The remainder of this paper is divided into four parts. In Sec. II we describe the linear combination of atomic orbitals (LCAO) formalism which underlies all our calculations. In Sec. III we present the details of our numerical work for the valence-band spectra of Si surfaces, and in Sec. IV we present and discuss our results in comparison with the data of Houston, Lagally, and Moore.[2] Finally, we summarize our conclusions in Sec. V.

II. LCAO THEORY OF VALENCE-BAND AUGER LINE SHAPES

In this section, expressions are derived for valence-band Auger line shapes within a tight-binding or LCAO picture of a solid surface. The use of a localized representation for the valence bands of the solid is particularly appropriate since the Auger effect involves the decay of a well-localized core hole, and since the largest contributions to the Coulombic matrix elements, which enter the Auger transition rate calculation, come from the immediate vicinity of the decaying hole.

To begin we sketch the derivation of a general independent-electron expression for the electron current which arrives at a detector at $\vec{R}$ with energy between E and $E+dE$, due to the Auger decay of a core hole in an atom at $\vec{R}_0$. We consider the case of a core-valence-valence transition first. The reduction of our result to that for a core-core-valence transition is trivial and is carried out at the end of this section.

The easiest way to proceed is by means of

Fermi's golden rule, according to which the differential current $R^2 j(\hat{R}, E)$ [or equivalently the differential inverse lifetime $d^2(1/\tau)/dE\, d\Omega$] may be written in the form

$$R^2 j\left(\hat{R}, E_k = \frac{\hbar^2 k^2}{2m}\right) = \frac{2\pi}{\hbar}\frac{k^2}{(2\pi)^3}\frac{dk}{dE_k}\sum_s |\mathfrak{M}_{\hat{R},s,c}|^2 \delta(E_k - E_s + E_c). \tag{2.1}$$

Here $\mathfrak{M}$ is the matrix element of the Coulomb interaction which causes the decay and the subscripts s and c refer, respectively, to the two-hole states of the solid, of energy E_s, and the core state which is decaying, of energy E_c.

In order to evaluate $\mathfrak{M}_{\hat{R},s,c}$ explicitly we assume that our solid has the geometry of a crystalline film, and for simplicity we neglect all spin-orbit coupling. Thus our valence-band states are labeled by the momentum along the surface $\vec{k}''$, a band index n, and the spin orientation σ equal to ± 1. The final (Auger) electron wave function is specified by its momentum along the surface $\vec{k}_f''$, its energy $E_f \equiv \hbar^2 k_f^2/2m$, and its spin orientation σ_f. Finally, the core-hole wave function is assumed to have angular momentum $L_i = (l_i, m_i)$ and spin orientation $\sigma_i = \pm 1$. Its energy is defined to be E_c, as noted above.

Having specified the quantum numbers of our solid's states explicitly, we write the Coulomb interaction Hamiltonian in the form

$$H^{\text{int}} = \sum_{\sigma_1,\sigma_2}\sum_{n_1,n_2}\sum_{\vec{k}_1'',\vec{k}_2'' \subset \text{2D BZ}} \int \frac{d^2k_f''}{(2\pi)^2} \mathfrak{M}_{\vec{k}_f'',E_f;L_i;\vec{k}_1'',n_1;\vec{k}_2'',n_2}\, c^\dagger_{\vec{k}_f'',E_f,\sigma_2} c^\dagger_{L_i,\sigma_1} c_{\vec{k}_1'',n_1,\sigma_1} c_{\vec{k}_2'',n_2,\sigma_2} + \text{H.c.}, \tag{2.2}$$

where the matrix element $\mathfrak{M}$ is given by

$$\mathfrak{M}_{\vec{k}_f'',E_f;L_i;\vec{k}_1'',n_1,\vec{k}_2'',n_2} = \int d^3r_1\, d^3r_2\, \psi^*_{\vec{k}_f'',E_f}(\vec{r}_2)\psi^*_{L_i}(\vec{r}_1)\frac{e^2}{|\vec{r}_1 - \vec{r}_2|}\psi_{\vec{k}_1'',n_1}(\vec{r}_1)\psi_{\vec{k}_2'',n_2}(\vec{r}_2), \tag{2.3}$$

where the $c^\dagger$'s and c's are creation and annihilation operators, and where the abbreviation 2D BZ means "two-dimensional Brillouin zone." At the same time we take the initial and final states in the Auger decay to be of the forms, respectively,

$$|\psi^{\text{init}}\rangle = c_{L_i,\sigma_i}|0\rangle, \tag{2.4}$$

and

$$|\psi^{\text{final}}\rangle = c^\dagger_{\vec{k}_f'',E_f,\sigma_f} c_{\vec{k}_1'',n_1,\sigma_1} c_{\vec{k}_2'',n_2,\sigma_2}|0\rangle, \tag{2.5}$$

where $|0\rangle$ is the Slater determinant corresponding to the solid's filled Fermi sea.

We now use Eqs. (2.2)–(2.5) to evaluate the Auger matrix element $\mathfrak{M}_{\hat{R},s,c}$ of Eq. (2.1). We obtain

$$\mathfrak{M}_{\hat{R},s,c} \equiv \langle\psi^{\text{final}}|H^{\text{int}}|\psi^{\text{init}}\rangle = \mathfrak{M}_{\vec{k}_f'',E_f;L_i;\vec{k}_1'',n_1;\vec{k}_2'',n_2} \times \delta_{\sigma_1,\sigma_i}\delta_{\sigma_2,\sigma_f} - \mathfrak{M}_{\vec{k}_f'',E_f;L_i;\vec{k}_2'',n_2;\vec{k}_1'',n_1}\delta_{\sigma_1,\sigma_f}\delta_{\sigma_2,\sigma_i}. \tag{2.6}$$

Substituting Eq. (2.6) into Eq. (2.1), interpreting the sum on s to be a sum on $\vec{k}_1''$, $\vec{k}_2''$, n_1, and n_2, averaging on the spin orientation of the initial hole and summing on that of the final electron, we obtain the expression for $R^2 j(\hat{R}, E_f)$,

$$R^2 j(\hat{R}, E_f) = \left(\frac{m}{2\pi\hbar^2}\right)^2 \frac{\hbar k_f}{m}\frac{1}{2}\sum_{\vec{k}_1'',\vec{k}_2'' \subset \text{2D BZ}}\sum_{n_1,n_2}\langle\mathfrak{M}^2(\vec{k}_f'', E_f; L_i; \vec{k}_1'', n_1; \vec{k}_2'', n_2)\rangle \delta(E_f - E_{\vec{k}_1'',n_1} - E_{\vec{k}_2'',n_2} + E_c), \tag{2.7}$$

where

$$\langle\mathfrak{M}^2(\vec{k}_f'', E_f; L_i; \vec{k}_1'', n_1; \vec{k}_2'', n_2)\rangle$$

is defined by

$$\langle\mathfrak{M}^2(\vec{k}_f'', E_f; L_i; \vec{k}_1'', n_1; \vec{k}_2'', n_2)\rangle \equiv 2\left(|\mathfrak{M}_{\vec{k}_f'',E_f;L_i;\vec{k}_1'',n_1;\vec{k}_2'',n_2}|^2 + |\mathfrak{M}_{\vec{k}_f'',E_f;L_i;\vec{k}_2'',n_2;\vec{k}_1'',n_1}|^2\right) - \left(\mathfrak{M}_{\vec{k}_f'',E_f;L_i;\vec{k}_1'',n_1;\vec{k}_2'',n_2}\mathfrak{M}^*_{\vec{k}_f'',E_f;L_i;\vec{k}_2'',n_2;\vec{k}_1'',n_1} + \text{c. c.}\right). \tag{2.8}$$

The over-all factor of $\frac{1}{2}$ in front of the $\vec{k}_1''$ and $\vec{k}_2''$ integrals in Eq. (2.7) takes account of the fact that the state with holes labeled by $(\vec{k}_1'', n_1)$ and $(\vec{k}_2'', n_2)$ is, by virtue of the indistinguishability of electrons, identical to the state in which the holes are labeled by $(\vec{k}_2'', n_2)$ and $(\vec{k}_1'', n_1)$.[5] The reason that the cross terms in Eq. (2.8) are not multiplied by 2 is that the exchange processes to which they correspond can only occur if $\sigma_i = \sigma_f$.

The final steps in calculating a general expression for an Auger line shape are to integrate on the exit angle of the Auger electron and to average over the orientation of the orbital angular momentum of the initial core hole. These steps lead to the expression

$$R^2J(E_f)\equiv\left\langle \int d\hat{R}\, j(\hat{R},E_f)\right\rangle_{m_i}$$

$$=\frac{m}{2\hbar^3}\frac{1}{2l_i+1}\sum_{m_i=-l_i}^{l_i}\int\frac{d^2k_f''}{(2\pi)^2}\frac{\Theta(k_f^2-k_f''^2}{(k_f^2-k_f''^2)^{1/2}}$$

$$\times\sum_{n_1,n_2}\sum_{\vec{k}_1'',\vec{k}_2''\subset 2D\ BZ}\langle\mathfrak{M}^2(\vec{k}_f'',E_f;L_i;\vec{k}_1'',n_1;\vec{k}_2'',n_2)\rangle\,\delta(E_f-E_{\vec{k}_1'',n_1}-E_{\vec{k}_2'',n_2}+E_c) \tag{2.9}$$

for $R^2J(E_f)$, the total number of Auger electrons emitted with energies between E_f and E_f+dE_f.

We now wish to evaluate Eq. (2.9) explicitly within the LCAO approximation. To begin, we write our valence-band wave functions in the LCAO form

$$\psi_{\vec{k}_j'',n_j}(r)=\frac{1}{\sqrt{N}}\sum_{\vec{R}_i,L_j}e^{i\vec{k}_j''\cdot\vec{R}_i''}c_{n_j,L_j}(\vec{k}_j'',Z_i)u_{L_j}(\vec{r}-\vec{R}_i), \tag{2.10}$$

where the atoms of the crystal film are located at the sites $\vec{R}_i\equiv(\vec{R}_i'',Z_i)$ and where the $u_{L_j}(\vec{r}-\vec{R}_i)$ are localized orbitals centered on these sites. The u_{L_j} are assumed to be normalized to 1. N is the number of two-dimensional unit cells which comprise the crystal. Using Eq. (2.10), the matrix elements of Eq. (2.3) which appear in Eq. (2.8) can be written in the form

$$\mathfrak{M}_{\vec{k}_f'',E_f;L_i;\vec{k}_1'',n_1;\vec{k}_2'',n_2}=\frac{1}{N}\sum_{\vec{R}_1,\vec{R}_2,L_1,L_2}e^{i(\vec{k}_1''\cdot\vec{R}_1''+\vec{k}_2''\cdot\vec{R}_2'')}c_{n_1,L_1}(\vec{k}_1,Z_1)\,c_{n_2,L_2}(\vec{k}_1,Z_2)\mathfrak{M}_{\vec{k}_f'',E_f;L_i,L_1,L_2}(\vec{R}_0,\vec{R}_1,\vec{R}_2), \tag{2.11}$$

where,

$$\mathfrak{M}_{\vec{k}_f'',E_f;L_i,L_1,L_2}(\vec{R}_0,\vec{R}_1,\vec{R}_2)\equiv\int d^3r_1\,d^3r_2\,\psi_{\vec{k}_f'',E_f}(r_2)\,\psi_{L_i}(\vec{r}_1-\vec{R}_0)\frac{e^2}{|\vec{r}_1-\vec{r}_2|}u_{L_1}(\vec{r}_1-\vec{R}_1)u_{L_2}(\vec{r}_2-\vec{R}_2). \tag{2.12}$$

In Eq. (2.12) the wave function of the decaying core hole has been rewritten as $\psi_{L_i}(\vec{r}_1-\vec{R}_0)$ to make explicit the location R_0 of the atom in which the hole exists.

We proceed by assuming that $\psi_{L_i}(\vec{r}_1-\vec{R}_0)$ is highly localized in space. As a consequence it is immediately obvious that the terms in Eq. (2.11) for which $\vec{R}_1\neq\vec{R}_0$ will be very small. These terms are therefore neglected in what follows. It is also easy to show[6] that terms with $\vec{R}_2\neq\vec{R}_0$ are generally small compared to those with $\vec{R}_2=\vec{R}_0$. [The leading contributions to $\mathfrak{M}$ are of $O(|\vec{R}_0-\vec{R}_2|^{-3})$ as $|R_0-R_2|$ becomes large compared to an atomic radius.] Thus to a first approximation we retain only those terms in Eq. (2.11) for which $\vec{R}_1=\vec{R}_2=\vec{R}_0$, and obtain

$$\mathfrak{M}_{\vec{k}_f'',E_f;L_i;\vec{k}_1'',n_1;\vec{k}_2'',n_2}=e^{i(\vec{k}_1''+\vec{k}_2'')\cdot\vec{R}_0}\frac{1}{N}\sum_{L_1L_2}c_{n_1,L_1}(\vec{k}_1'',Z_0)\,c_{n_2,L_2}(\vec{k}_2'',Z_0)\mathfrak{M}_{\vec{k}_f'',E_f;L_i,L_1,L_2}(\vec{R}_0,\vec{R}_0,\vec{R}_0). \tag{2.13}$$

We now pursue the idea that the main contributions to the Auger matrix element come from the immediate vicinity of the core hole. This idea implies that whatever the differences might be between the $u_{L_j}(\vec{r})$ which best describe the wave functions of a solid and the corresponding orbitals of isolated atoms, these differences will be of minor importance in evaluating the Auger matrix element. Thus the only significant difference between $\mathfrak{M}_{\vec{k}_f'',E_f;L_i,L_1,L_2}(\vec{R}_0,\vec{R}_0,\vec{R}_0)$ and an atomic Auger matrix element is that the final electron wave function $\psi_{\vec{k}_f'',E_f}(\vec{r})$ contains contributions due to the scattering of this electron from the surrounding ions and in the ambient electron sea.

However, in the present calculation, we are only interested in the angle-integrated Auger current $R^2J(E)$. Thus it is reasonable to assume that the effects of elastic scattering of the Auger electron from ion cores will be small, i.e., that although this scattering may have a dramatic effect on the angular distribution of Auger intensity it will not severely affect the number of Auger

electrons which emerge from the crystal relative to the number of them which are trapped inside it. Thus to calculate $R^2J(E_f)$ we assume that $\psi_{\vec{k}_f'',E_f}(\vec{r})$ may be taken to be an atomic final-state wave function, centered at $\vec{R}_0$, times a phenomenological attenuation factor that accounts for the loss of Auger electrons due to *inelastic* scattering processes. Specifically, we write

$$\psi_{\vec{k}_f'',E_f}(\vec{r}) = \psi^{(\mathrm{AT})}_{\vec{k}_f'',E_f+V_0}(\vec{r}-\vec{R}_0)\exp\{-(Z_0/\lambda)[(E+V_0)/(E+V_0-\hbar^2k_f''^2/2m)]^{1/2}\}, \tag{2.14}$$

where λ is the inelastic mean free path at energy E_f, V_0 is our solid's inner potential, and thus the square-root term in the exponential is the secant of the Auger electron escape angle inside the crystal. $\psi^{(\mathrm{AT})}_{\vec{k}_f'',E_f+V_0}(\vec{r}-\vec{R}_0)$ is the final electron wave function appropriate to an atomic Auger transition. It is in general a distorted-wave wave function satisfying incoming-wave boundary conditions asymptotically as $|\vec{r}-\vec{R}_0|\to\infty$.[7] We evaluate it at energy E_f+V_0 rather than at E_f to take account of the increased kinetic energy of the Auger electron when it is inside the solid.

We now substitute Eq. (2.14) into Eq. (2.13), and the latter into Eq. (2.9). This procedure yields the expression for the Auger current emanating from Z_0:

$$R^2J(E_f,Z_0) = \sum_{L_1,L_2,L_1',L_2'}\int d\omega\, F_{L_1,L_1'}(E_f-\omega,Z_0) \times F_{L_2,L_2'}(E_c+\omega,Z_0) \times W_{L_1,L_1',L_2,L_2'}(E_f,Z_0), \tag{2.15}$$

wherein the $F_{L,L'}(E,Z)$ are local density-of-states matrices, defined by

$$F_{L,L'}(E,Z) \equiv \frac{1}{N}\sum_{n,\vec{k}''\subset 2\mathrm{D\ BZ}} \delta(E-E_{\vec{k}'',n})c_{n,L}(\vec{k}'',Z) \times c^*_{n,L'}(\vec{k}'',Z), \tag{2.16}$$

and the quantity $W_{L_1,L_1',L_2,L_2'}(E,Z)$ is given by

$$W_{L_1,L_1',L_2,L_2'}(E_f,Z_0) \equiv \frac{m}{\hbar^2}\frac{1}{2l_i+1}\sum_{m_i}\int \frac{d^2k_f''}{(2\pi)^2}\frac{\Theta(k_f^2-k_f''^2}{(k_f^2-k_f''^2)^{1/2}}\exp\left[-\left(\frac{2Z_0}{\lambda}\right)\left(\frac{E_f+V_0}{(E_f+V_0-\hbar^2k_f''^2/2m)}\right)^{1/2}\right] \times\{[M^{(\mathrm{AT})}_{\vec{k}_f'',E_f;L_i,L_1L_2}(M^{(\mathrm{AT})*}_{k_f'',E_f;L_i,L_1',L_2'} - \tfrac{1}{2}M^{(\mathrm{AT})*}_{k_f'',E_f;L_i,L_2',L_1'})] + (L_1,L_1' \rightleftarrows L_2,L_2')\}. \tag{2.17}$$

In Eq. (2.17), the $M^{(\mathrm{AT})}$ are given by

$$M^{\mathrm{AT}}_{\vec{k}_f'',E_f;L_i,L_1,L_2} \equiv \int d^3r_1\, d^3r_2\, \psi^*_{\vec{k}_f'',E_f+V_0}(\vec{r}_2)\psi^*_{L_i}(\vec{r}_2)\frac{e^2}{|\vec{r}_1-\vec{r}_2|}u_{L_1}(\vec{r}_1)u_{L_2}(\vec{r}_2). \tag{2.18}$$

We proceed to simplify somewhat further by expanding the $\psi^{(\mathrm{AT})*}_{\vec{k}_f'',E_f+V_0}(\vec{r})$ in partial waves. This expansion permits the direct evaluation of the $\vec{k}_f''$ integral in Eq. (2.17). Thus we write $\psi^{(\mathrm{AT})*}_{\vec{k}_f'',E_f+V_0}(\vec{r})$ in the form[8]

$$\psi^{(\mathrm{AT})*}_{\vec{k}_f'',E+V_0}(\vec{r}) = \frac{4\pi}{p_f r}\sum_{l,m} Y_{lm}(\hat{p}_f)\exp\left\{i\left[\delta_l - \tfrac{1}{2}\pi l - \arg\Gamma\left(l+1+\frac{iZ}{p_f a_0}\right)\right]\right\}F_l(p_f r)Y^*_{l,m}(\hat{r}), \tag{2.19}$$

where

$$\vec{p}_f \equiv (\vec{k}_f'', [2m(E+V_0)/\hbar^2 - k_f''^2]^{1/2}), \tag{2.20}$$

and where $\Gamma(z)$ is the gamma function (of complex argument), a_0 is the Bohr radius, and Z is the charge on the atom at Z_0 after the Auger process has occurred. In our calculations, as is discussed below, Z was set equal to 2. $F_l(p_f r)$ in Eq. (2.20) is the lth partial-wave solution to the radial Schrödinger equation for the Auger electron. As $p_f r\to\infty$, $F_l(p_f r)$ behaves according to

$$F_l(p_f r) \xrightarrow[p_f r\to\infty]{} \sin\left[p_f r - \tfrac{1}{2}\pi l + \frac{Z}{p_f a_0}\ln 2p_f r - \arg\Gamma\left(l+1+\frac{iZ}{p_f a_0}\right) + \delta_l\right]. \tag{2.21}$$

We make use of the expansion of Eq. (2.19) by noting that

$$\int d^2k_f'' \frac{\Theta(k_f^2 - k_f''^2)}{(k_f^2 - k_f''^2)^{1/2}} \exp\left[-\left(\frac{2Z_0}{\lambda}\right)\left(\frac{E_f + V_0}{E_f + V_0 - \hbar^2 k_f''^2/2m}\right)^{1/2}\right] Y_{l_1,m_1}(\hat{p}_f) Y^*_{l_2,m_2}(\hat{p}_f) = \delta_{m_1 m_2} B_{l_1,l_2,m_1}(E_f, Z_0), \quad (2.22)$$

where $B_{l_1,l_2,m}(E_f,Z_0)$ is defined by

$$B_{l_1,l_2,m}(E_f,Z_0) = \frac{1}{2}\left(\frac{2mE_f}{\hbar^2}\right)\frac{(2l_1+1)(2l_2+1)(l_1-m)!\,(l_2-m)!}{(l_1+m)!\,(l_2+m)!}\Bigg)^{1/2} \int_0^1 dx\, P_{l_1}^m(y(x)) P_{l_2}^m(y(x)) e^{-2Z_0/\lambda y(x)}, \quad (2.23)$$

with

$$y(x) \equiv [(E_f x^2 + V_0)/(E_f + V_0)]^{1/2}. \quad (2.24)$$

The $P_l^m(y)$ are of course associated Legendre polynomials.

Substituting Eq. (2.22) into Eq. (2.17), we find that

$$W_{L_1,L_1',L_2,L_2'}(E_f,Z_0) = \frac{4m}{\hbar^3}\frac{1}{2l_i+1}\sum_{m_i}\sum_{m_f,l_{f_1},l_{f_2}} B_{l_{f_1},l_{f_2},m}(E_f,Z_0) \times \{[M_{l_{f_1},m_f;L_i,L_1,L_2}(M^*_{l_{f_2},m_f;L_i,L_1',L_2'} - \tfrac{1}{2}M^*_{l_{f_2},m_f;L_i,L_2',L_1'})] + L_1,L_1' \rightleftharpoons L_2,L_2'\}, \quad (2.25)$$

where the atomic Auger matrix elements $M_{l_f,m_f;L_i,L_1,L_2}$ are defined by

$$M_{l_f,m_f;L_i,L_1,L_2} \equiv \int d^3r_1\, d^3r_2 \frac{\exp\{i[\delta_l - \pi l/2 - \arg\Gamma(l+1+iZ/p_f a_0)]\}}{p_f r_2} F_{l_f}(p_f r_2) Y^*_{l_f,m_f}(\hat{r}_2) \times \psi^*_{L_i}(\vec{r}_1)\frac{e^2}{|\vec{r}_1 - \vec{r}_2|} u_{L_1}(\vec{r}_1) u_{L_2}(\vec{r}_2). \quad (2.26)$$

Equations (2.15)–(2.17) and (2.21)–(2.26) constitute our final reduction of our LCAO expression for the Auger CVV line shape $R^2J(E_f,Z_0)$. In our calculations, discussed in the next sections of this paper, we have taken the distribution of core holes within a few mean free paths of the surface to be uniform. Thus what we have actually calculated is

$$R^2J(E_f) \equiv \sum_{Z_0} R^2J(E_f,Z_0), \quad (2.27)$$

the sum of the contributions from the first several layers of the crystal.

The last question we wish to treat in this section is what modification of the above equations are necessary for the case of a core-core-valence (CCV) transition. The answer is simply that in addition to using an appropriate $u_L(r)$ for the core wave function in Eq. (2.26), we must allow *either* of the local density-of-states matrices $F_{L,L'}$ in Eq. (2.15) to equal the core-level density-of-states matrix

$$\delta_{L,L'}\delta_{L_{c'},L}\delta(E - E_{c'}), \quad (2.28)$$

where $L_{c'}$ and $E_{c'}$ are the angular momentum and energy of the upper core state in the CCV transition. Thus we find for $R^2J(E_f,Z_0)$ the expression

$$R^2J(E_f,Z) = 2\sum_{L,L',m_{c'}} F_{L,L'}(E_f - E_{c'} + E_c) \times W_{L_{c'},L_{c'},L,L'}(E_f,Z_0). \quad (2.29)$$

The factor 2 comes from allowing either of the F's to represent the upper core level, and using the symmetry of $W_{L_1,L_1',L_2,L_2'}(E,Z)$ under the interchange $L_1,L_1' \rightleftharpoons L_2,L_2'$.

III. NUMERICAL CALCULATIONS OF VALENCE-BAND AUGER LINE SHAPES FOR Si (111), (100), AND (110) SURFACES

In this section we present the elements of our numerical calculations. Our results are discussed in Sec. IV. There are two sorts of quantities that must be calculated in order to evaluate an Auger current via Eq. (2.15), namely local density-of-states matrices [the $F_{L,L'}(E,Z)$ of Eq. (2.17)] and atomic matrix elements [defined in Eq. (2.27)]. The $F_{L,L'}(E,Z)$ are computed in our work on the basis of the empirical tight-binding Hamiltonian of Pandey and Phillips,[9] which gives an excellent fit to bulk pseudopotential band-structure calculations for Si, as well as to surface band positions found in the first-principles Si surface electronic structure calculations of Appelbaum and Hamann.[10]

We replace the δ-function integration in Eq. (2.17) by a density-of-states histogram, with energy boxes 0.3 eV wide. For the Si(111) surface we use a $\vec{k}''$ mesh [in Eq. (2.17)] of 66 points in the irreducible twelfth of the two-dimensional Brillouin zone. For the (100) and (110) surfaces the $\vec{k}''$ mesh comprises 49 points in the irreducible fourth of the 2D BZ. In none of our calculations have we yet included any surface reconstruction. We have, however, included surface relaxation. In the (111) case we take the separation of the two outermost Si layers to be 0.58 times its bulk value, and for the (100) surface, 0.63 times its bulk value. For the (110) surface, of course, atoms of both sublattices of the diamond structure are in the first layer and no relaxation of this layer relative to the second layer is considered. All of our calculations are carried out for crystal films having 20 layers of Si atoms. In the (110) case this statement involves counting each actual layer as two layers.

Our calculation of the matrix elements of Eq. (2.26) takes full advantage of the symmetry of the atomic orbitals involved. Thus writing

$$\psi_{L_i}(\vec{r}) = (1/r)R_{l_i}(r)Y_{l_i m_i}(\Omega) \tag{3.1}$$

and

$$u_{L_j}(\vec{r}) = (1/r)R_{l_j}(r)Y_{l_j m_j}(\Omega), \tag{3.2}$$

and making use of the identity

$$\frac{1}{|\vec{r}_1 - \vec{r}_2|} = 4\pi \sum_{\kappa=0}^{\infty} \sum_{\beta=-\kappa}^{\kappa} \frac{1}{2\kappa+1} \frac{r_<^\kappa}{r_>^{\kappa+1}} Y^*_{\kappa\beta}(\Omega_1) Y_{\kappa\beta}(\Omega_2), \tag{3.3}$$

we write

$$M_{l_f,m_f;L_i,L_1,L_2} \equiv e^2 \left(\frac{\pi}{p_f}\right)^{1/2} \exp\left\{ i\left[\delta_l - \tfrac{1}{2}\pi l - \arg\Gamma\left(l+1+\frac{iZ}{p_f a_0}\right)\right]\right\} \sum_\kappa \mathcal{R}_\kappa(l_f,l_i,l_1,l_2) A_{l_f,m_f;L_i,L_1,L_2}(\kappa) \tag{3.4}$$

where $A_{l_f,m_f;L_i,L_1,L_2}(\kappa)$ is the angular part of the matrix element, given by

$$A_{l_f,m_f;L_i,L_1,L_2}(\kappa) \equiv \frac{4\pi}{2\kappa+1} \sum_{\beta=-\kappa}^{\kappa} \int d\Omega_1 Y^*_{l_i m_i}(\Omega_1) Y_{l_1 m_1}(\Omega_1) Y^*_{\kappa\beta}(\Omega_1) \int d\Omega_2 Y^*_{l_f m_f}(\Omega_2) Y_{l_2 m_2}(\Omega_2) Y_{\kappa\beta}(\Omega_2), \tag{3.5}$$

and where $\mathcal{R}_\kappa(l_f,l_i,l_1,l_2)$ is a dimensionless radial integral given by

$$\mathcal{R}_\kappa(l_f,l_i,l_1,l_2) \equiv \int dr_1\, dr_2 \frac{r_<^\kappa}{r_>^{\kappa+1}} \frac{F_{l_f}(p_f r_2)}{(\pi p_f)^{1/2}} \times \mathcal{R}_{l_2}(r_2)\mathcal{R}_{l_1}(r_1)\mathcal{R}_{l_i}(r_1). \tag{3.6}$$

The evaluation of the angular integrals is a straightforward exercise in vector-coupling coefficients. Results of this exercise are given in Appendix A. Here the only feature of $A_{l_f,m_f;L_i,L_1,L_2}(\kappa)$ that we wish to discuss is that it expresses selection rules which are typically not considered in DOS models of Auger transitions but which, as is shown below, can play a significant role in determining an Auger line shape. The parity selection rule, implicit in Eq. (3.5) requires

$$l_i + l_1 + \kappa \text{ even integer} \tag{3.7a}$$

and

$$l_f + l_2 + \kappa \text{ even integer}. \tag{3.7b}$$

At the same time angular momentum conservation requires that

$$\beta = m_1 - m_i = m_f - m_2, \tag{3.8}$$

and also that

$$|l_i - \kappa| \le l_1 \le l_i + \kappa \tag{3.9}$$

and

$$|l_2 - \kappa| \le l_f \le l_2 + \kappa. \tag{3.10}$$

In Table I we show the values of L_1, L_2, and L_f allowed by Eqs. (3.7)–(3.10) for a specific case, the $L_{2,3}VV$ Auger line of Si. In this case of course $l_i = 1$. The table reveals the following interesting facts:

(i) If $l_1 + l_2 = 0$, i.e., if the Auger decay occurs

TABLE I. Quantum numbers for allowed $L_{2,3}VV$ transitions in Si. The meaning of the punctuation in the table is illustrated by the following example. If $l_1 = 1$, $l_2 = 0$, and $l_f = 2$, then if $m_1 + m_2 = 1$, m_f can equal 2, 1, or 0. If $m_1 + m_2 = 0$ then $m_f = 1$, 0, or −1, etc.

l_1	l_2	m_1+m_2	l_f	m_f	No. channels
0	0	0	1	1,0,−1	3
1	0	1;0;−1	0	0;0;0	3
1	0	1;0;−1	2	2,1,0;1,0,−1;0,−1,−2	9
0	1	1;0;−1	0	0;0;0	3
0	1	1;0;−1	2	2,1,0;1,0,−1;0,−1,−2	9
1	1	2	1;3	1;3,2,1	4
1	1	1	1;3	1,0;2,1,0	10
1	1	0	1;3	1,0,−1;1,0,−1	18
1	1	−1	1;3	0,−1;0,−1,−2	10
1	1	−2	1;3	−1;−1,−2,−3	4

via a pair of s electrons in the valence band, there are just three allowed decay channels (corresponding respectively to $m_i = 1, 0$, and -1).

(ii) If $l_1 + l_2 = 1$, i.e., if the decay occurs via an s-p configuration, there are now 24 allowed decay channels, or 4 channels per s-p configuration.

(iii) Finally, if $l_1 + l_2 = 2$, so that the decay occurs via a p-p valence configuration, there are 46 allowed decay modes, or 5.1 per p-p configuration.

These facts show that kinematics (i.e., conservation laws) favor the decay of the $L_{2,3}$ hole via p-p configurations, an effect which goes in the direction of resolving the discrepancy between Houston, Lagally, and Moore's data and the DOS model (cf. Figs. 1 and 2). In Fig. 3 we illustrate the quantitative significance of this kinematic effect. The "kinematics" curve of Fig. 3 is obtained [for the Si(111) surface] by setting all the allowed matrix elements in Eq. (2.25) equal to 1 and all the forbidden ones equal to 0, and then by calculating $R^2 J(E_f)$ via Eq. (2.16). Note that this calculation leads to a curve which is in much better agreement with the data than the corresponding DOS model curve of Fig. 1. The improved agreement stems, of course, from the enhanced contributions of the p-like (upper) part of the Si valence band when selection rules are considered.

We conclude this section with a brief discussion of the radial matrix elements of Eq. (3.6). These elements were calculated using Herman-Skillman wave functions for Si.[11] The final electron wave function $F_{l_f}(p_f r)$ was calculated assuming that the outgoing electron sees a doubly charged Si ion as it leaves the crystal. While we believe that this assumption is not of significant quantitative importance (particularly for the higher energy LVV Auger lines), we think it is reasonable because of the following argument: The characteristic time for the neutralization of valence band holes in Si is of the order of $\hbar/W$, where W is the valence-band width (~ 12.5 eV). In this time an Auger electron travels a distance greater than $(\hbar/W)(2E/m)^{1/2}$. For a 100-eV Auger electron, this distance is[12] $d \simeq a_0 (E/\mathcal{R})^{1/2} (\mathcal{R}/W) \approx 1.56$ Å which is about $\frac{2}{3}$ the Si-Si nearest-neighbor distance in bulk Si, and which is thus far enough from a Si nucleus that the behavior of the final-electron wave function no longer affects the Auger matrix element significantly. Therefore, by the time any neutralization of the Si^{++} can occur the Auger electron is outside the region where the nature of the ionic potential is important. For an $L_1 L_{2,3} V$ Auger electron this argument also applies although d is now only ≈ 0.5 the Si-Si bond length. Consequently, we have calculated our Auger electron wave functions using the potential due to a Si^{++}.

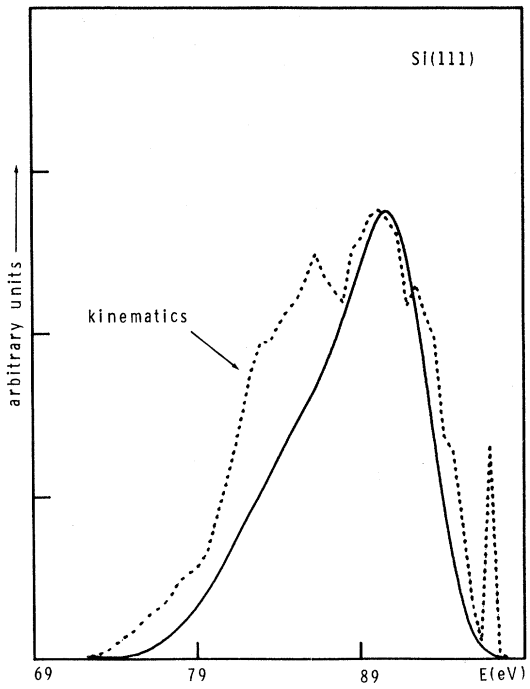

FIG. 3. Comparison of $L_{2,3}VV$ Auger line shape for Si(111) (solid line) with "kinematic" line shape obtained by setting all allowed matrix elements in Eq. (2.15) equal to 1 and all forbidden ones equal to zero. λ was taken to equal 7 Å.

Values of the $\mathcal{R}_k(l_f, l_i, l_1, l_2)$ are tabulated in Tables II and III, along with values of the phase shifts δ_l [cf. Eq. (2.21)] which one also needs to evaluate the total atomic matrix elements $[M_{l_f, m_f; L_i, L_1, L_2}$ of Eq. (2.26)] [cf. also Eq. (3.4)].

IV. $L_{2,3}VV$ AND $L_1 L_{2,3} VV$ AUGER LINE SHAPES FOR UNRECONSTRUCTED Si (111), (100), AND (110) SURFACES

In this section we present and discuss the results of our calculations for both the $L_{2,3}VV$ and $L_1 L_{2,3} V$ ("Coster-Kronig") Auger transitions for unreconstructed models of the (111), (100), and (110) surfaces of Si. We compare our results to data from annealed Si (111) and (100) crystal surfaces, taken recently by Houston, Lagally, and Moore.[2]

In Figs. 4–6 we show calculated and experimental $L_{2,3}VV$ spectra for the (111), (100), and (110) surfaces of Si. The most important result shown in the figures is the generally excellent agreement in overall line shape between theory and experiment for the two surfaces for which adequate data exist. The reason that the theoretical points agree so much more closely with experiment than did the weighted self-folds of the den-

TABLE II. (a) Magnitudes of dimensionless radial matrix elements for Si $L_{2,3}VV$ Auger transitions. (b) Sines and cosines of δ_l, the phase shift which appears in the asymptotic form of the final electron wave function [see Eq. (2.21)].

(a) Matrix elements for $L_{2,3}VV$ transitions

E (eV)	$R_1(1,1,0,0)$	$R_0(0,1,1,0)$	$R_1(0,1,0,1)$	$R_1(2,1,0,1)$	$R_2(2,1,1,0)$	$R_2(3,1,1,1)$	$R_0(1,1,1,1)$	$R_2(1,1,1,1)$
85	0.581×10^{-2}	-0.739×10^{-2}	-0.579×10^{-2}	0.070×10^{-2}	0.233×10^{-2}	1.045×10^{-2}	0.816×10^{-2}	0.417×10^{-2}
95	0.624	−0.723	−0.596	0.035	0.151	0.948	0.802	0.458
105	0.659	−0.711	−0.611	0.013	0.087	0.848	0.786	0.493
115	0.683	−0.696	−0.621	0.003	0.042	0.761	0.771	0.519

(b) Phase shifts for $L_{2,3}VV$ transitions

E (eV)	$\cos\delta_0$	$\sin\delta_0$	$\cos\delta_1$	$\sin\delta_1$	$\cos\delta_2$	$\sin\delta_2$	$\cos\delta_3$	$\sin\delta_3$
85	−0.6932	−0.7210	−0.9123	0.4095	0.2640	0.9645	0.8459	0.5334
95	−0.7201	−0.6939	−0.8976	0.4408	0.2634	0.9646	0.8372	0.5469
105	−0.7397	−0.6729	−0.8801	0.4747	0.2601	0.9656	0.8246	0.5657
115	−0.7635	−0.6458	−0.8648	0.5021	0.2621	0.9650	0.8189	0.5739

sities of states (WSFDOS's[3]) for Si (111) and (100), cf. Figs. 1 and 2, is that Auger decays involving two p-like valence electrons have large matrix elements compared to those involving either one or two s electrons. This fact is confirmed by the very close agreement, surface by surface, of calculated Auger line shapes and weighted self-folds of the p-like part of the DOS (the latter are not shown in Fig. 3 precisely because the agreement is so close). Incidentally the fact that Auger decays involving two p electrons have the largest matrix elements is not evident in Table II. It is the large angular matrix element associated with $R_0(1,1,1,1)$ that establishes the p electrons as most important.

The agreement between theory and experiment in Figs. 4 and 5 extends not only to the $L_{2,3}VV$ line shapes but also their positions. The energy scale in the theoretical calculations was fixed by assuming the $L_{2,3}$ level to lie 99.5 eV below the valence-band maximum, which is the energy of the $L_{2,3}$ x-ray emission edge. Since this experimental threshold energy presumably includes effects due to relaxation of valence electrons about a Si $2p$ hole, it is fair to say that we have phenomenologically included this many-electron relaxation effect in our independent-electron calculation. But it is also worthwhile noting that scarcely any (i.e., ≤ 1 eV) relaxation effect (e.g., due to two-hole repulsion) had to be assumed to give agreement between the theoretical and experimental $L_{2,3}VV$ line positions.[13]

In detail, of course, the agreement between the theoretical and experimental curves of Figs. 4 and 5 is not perfect. To begin a detailed comparison, note that the theoretical curves for the (111) and

TABLE III. (a) Magnitudes of dimensionless radial matrix elements for Si $L_1L_{2,3}VV$ Auger transitions. The notation $R_0(l_f,0,1_L,1_M)$ means that $l_1=1$ and is an L-shell (core) state while $l_2=1$ and is an M-shell (valence) state. (b) Sines and cosines of δ_l, the phase shift which appears in the final state wave function [cf. Eq. (2.21)].

(a) Matrix elements for $L_1L_{2,3}V$ transitions

E (eV)	$R_0(1,0,0,1)$	$R_0(1,0,1,0)$	$R_1(0,0,1_L,1_M)$	$R_1(0,0,1_M,1_L)$	$R_1(2,0,1_L,1_M)$	$R_1(2,0,1_M,1_L)$
46	2.10×10^{-2}	6.04×10^{-2}	4.29×10^{-2}	1.86×10^{-2}	1.27×10^{-2}	-0.693×10^{-2}
51	2.07	5.75	4.16	1.84	0.818	−0.749
56	2.04	5.47	4.03	1.81	0.401	−0.797
61	1.99	5.20	3.95	1.82	0.030	−0.852
66	1.97	4.98	3.85	1.80	−0.320	−0.898

(b) Phase shifts for $L_1L_{2,3}V$ transitions

E (eV)	$\cos\delta_0$	$\sin\delta_0$	$\cos\delta_1$	$\sin\delta_1$	$\cos\delta_2$	$\sin\delta_2$
40	−0.5251	−0.8510	−0.9845	0.1756	0.2843	0.9587
51	−0.5483	−0.8363	−0.9791	0.2036	0.2801	0.9600
56	−0.5685	−0.8227	−0.9730	0.2307	0.2775	0.9607
61	−0.5984	−0.8012	−0.9638	0.2667	0.2694	0.9630
66	−0.6130	−0.7901	−0.9561	0.2929	0.2657	0.9640

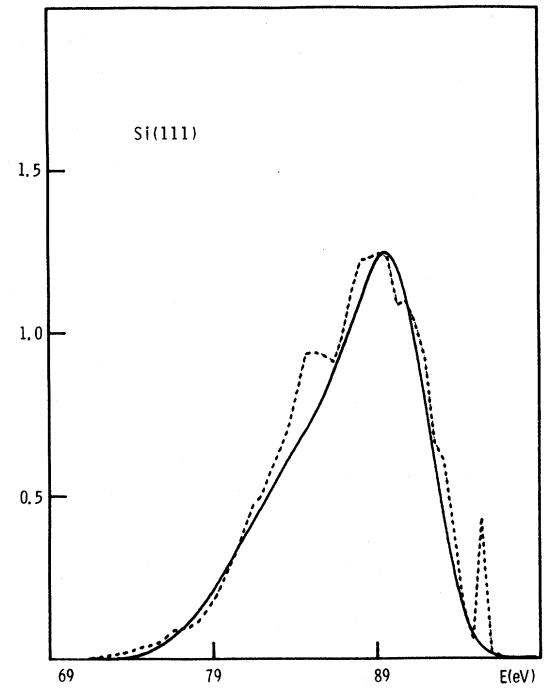

FIG. 4. Comparison of the $L_{2,3}VV$ Auger line shape for Si(111) (solid line) measured by Houston, Lagally, and Moore (Ref. 2) with that calculated using Eq. (2.15) together with actual atomic Auger matrix elements. λ was set equal to 7 Å in the calculation. The theoretical curve is shifted upward by 1 eV from that which would be obtained using the core-hole energy of -99.5 eV given by the $L_{2,3}$ x-ray emission threshold (see also Ref. 13). Units for the theory curve are $4\pi \times 10^{-4}\hbar^{-1}$.

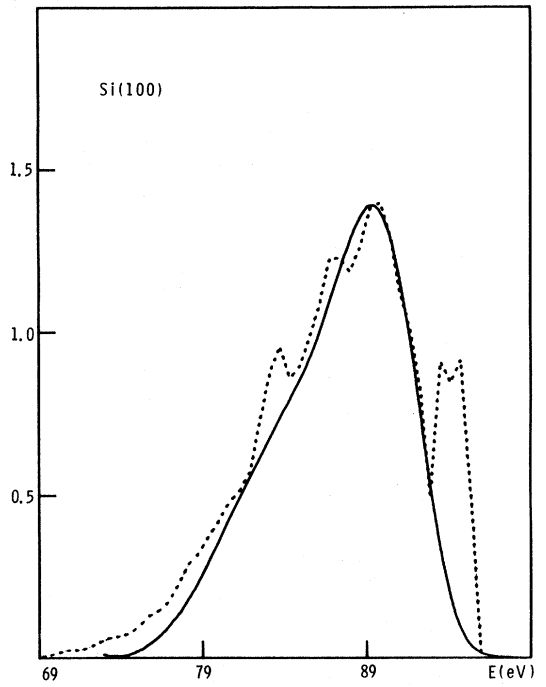

FIG. 5. Comparison of data (solid line) and full theory (dashed line) for the $L_{2,3}VV$ transition on Si(100). λ was taken to be 7 Å in the calculation. The theory curve is shifted downward by 0.7 eV relative to that which would be obtained using $E_c = -99.5$ eV (see also Ref. 13). Units for the theory curve are $4\pi \times 10^{-4}\hbar^{-1}$.

(100) surfaces show fairly sharp structure while the experimental curves do not. The most prominent structures in the theoretical curves are the narrow peaks on their high-energy sides (at about 95 eV). These peaks are due to Auger decays in which both the electron which falls into the core hole, and that which is detected, were originally located in a dangling-bond surface state. Thus, one obvious explanation of why these peaks are not present in the data is that Coulomb repulsion makes it very unlikely that two electrons will reside in a single dangling bond.[14] The absence of these peaks may therefore be a true many-electron or correlation effect, which is not taken into account in our independent-electron model. For the Si(100) surface there is another reason why we might expect the dangling-bond peak to be absent experimentally, namely that the experimental surface is 2×1 reconstructed. There is reason to believe that this reconstruction of the (100) surface results in a surface density of states with no sharp dangling-bond peak[15]—an idea which is in agreement with photoemission data also showing

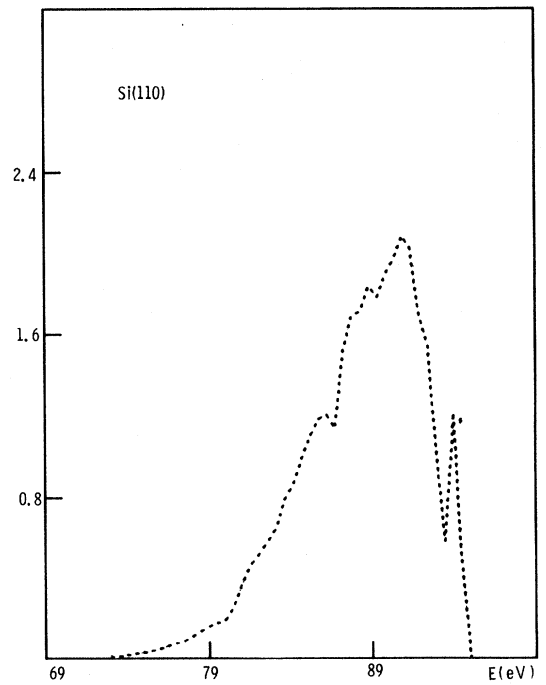

FIG. 6. Calculated $L_{2,3}VV$ Auger line shape for an ideal Si(110) surface with $\lambda = 7$ Å and $E_c = -99.5$ eV. Units for the ordinate are $4\pi \times 10^{-4}\hbar^{-1}$.

no such peak.[16]

The structure found in the theoretical curves at ~85 eV does seem to correspond to weak structure in the data. However the splitting of the theoretical peak at ~89 eV for the (100) surface has no counterpart in the data. The absence of this splitting may be due to the same broadening effect which is responsible for the difference between the fairly sharp structure in the theory curves at ~85 eV and the broad corresponding structure in the data.

This discussion makes clear that one of the fundamental features of the Si (as well as other) Auger line shape data which remains to be understood is the broadness of the structures which are observed. We may surmise that it is the thermalization of the holes left behind in the Auger decay which smears the structure in the line shape, and moreover that this thermalization involves electron-hole pair excitation (i.e., further Auger processes). This guess does account for the fact that the leading (high energy) edges of the theoretical and experimental $L_{2,3}VV$ line shapes agree quite well—since one would expect the lifetime of a hole near the valence-band maximum to be quite long. However, it leaves open the question of why structures in Auger spectra typically seem more smeared out than those which are seen in photoemission from the same material.

In conclusion it should be noted that the experimental $L_{2,3}VV$ curves for the (111) and (100) surfaces are virtually indistinguishable. This fact might be due to the smearing out of surface-related structures, as just discussed. It might indicate that there is a similarity between the reconstructed (111) and (100) surfaces.[17] Or it might indicate that at ~90 eV the Si inelastic mean free path is sufficiently large (we used $\lambda = 7$ Å in all of our calculations) that the data are dominated by the bulk properties of Si. We hope soon to be able to analyze data for Auger emission from atoms absorbed on Si. In this case we will be able to identify the region of space from which the data come with more confidence.

We turn our attention now to the $L_1L_{2,3}V$ "Coster-Kronig" transition for the (111), (100), and (110) surfaces. Theoretical points are compared to experimental data[2] in Figs. 7–10. The theoretical points here have been obtained by folding the $R^2J(E_f)$ curve obtained via the method of Secs. II

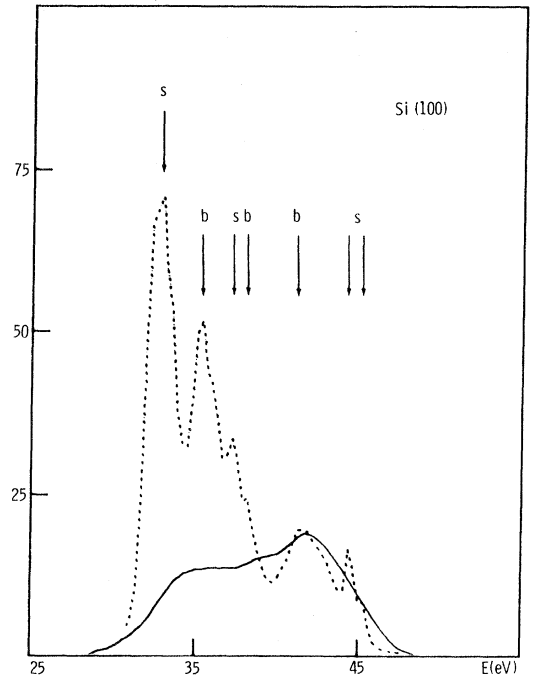

FIG. 7. Comparison of experimental (solid curve) and theoretical (dashed curve) $L_1L_{2,3}V$ Auger line shapes for Si(100). The features labeled s and b in the theoretical curves correspond, respectively, to peaks in the first layer and bulk Si density of states. The theoretical curve is shifted upward by 2.5 eV relative to where it would be if we used x-ray level positions for the L_1 and $L_{2,3}$ energies. Units for the theory curve are $4\pi \times 10^{-4}\hbar^{-1}$.

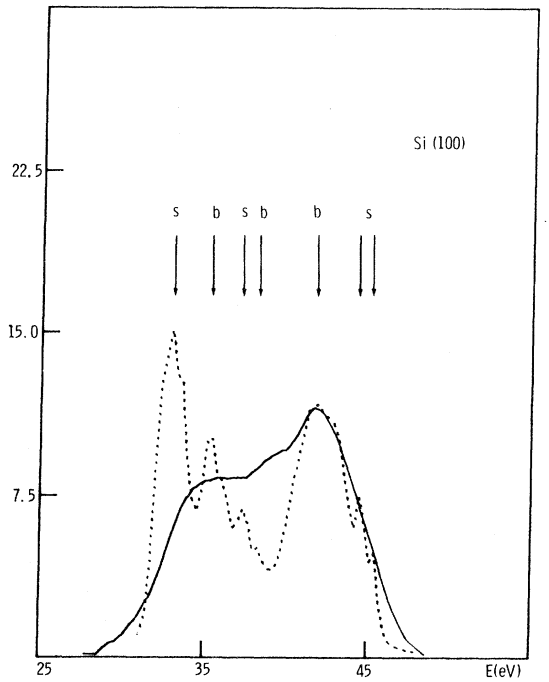

FIG. 8. Comparison of experimental (solid line) and theoretical (dashed line) $L_1L_{2,3}V$ Auger line shapes for Si(100) where the atomic matrix elements for transitions involving s-like valence electrons have been scaled down by a factor of 2.5. The theory curve is shifted upward by 2.5 eV relative to its position using x-ray energy levels. Units for this curve are $4\pi \times 10^{-4}\hbar^{-1}$.

and III with a Lorentzian of full width 0.5 eV, which accounts roughly for the lifetime broadening of a 2*s* hole in Si.[18] The agreement between theory and experiment [for Si(100)] in Fig. 7 is quite poor by contrast to that found in Fig. 5 for the $L_{2,3}VV$ line shape. We do find that the three peaks in the data agree in relative position with the "bulk" peaks in the theory [i.e., with those peaks which are attributable to the bulk Si DOS rather than to the DOS of the (100) surface]. However, there are obviously large discrepancies between the theoretical and experimental curves; notably:

(i) The theoretical curve shows considerably more structure than the experimental one. The dangling-bond peaks of the theory (at ~45 eV) are absent in the data. The same is true of the back-bond peaks [e.g., the peak at ~32 eV for the (100) surface].

(ii) The *s*-like (low energy) peaks are much weaker relative to the *p*-like peaks than they are in the theory.

Regarding the first discrepancy, it is clear at the outset that since we are here considering Auger transitions which involve only one valence electron, the Coulomb repulsion argument which was used to explain the absence of the dangling-bond peak in the $L_{2,3}VV$ spectrum is not relevant. Thus there remain two possible explanations of this discrepancy:

(a) The experimental line shape represents a broadened version of the one-electron theory result. Thus the uppermost peak in the data is as broad as it is because it corresponds not just to the highest-energy bulk peak in the theory but to both this bulk peak and that associated with the dangling bonds. A similar argument applies for the back-bond peaks. Alternatively,

(b) The dangling-bond peak should be absent for the reconstructed surface. This argument finds some support in theory[15] (to the extent that one has faith in the model used for the geometry of the reconstructed surface) and in photoemission data.[16] And it also applies for the back-bond peaks.

Turning to the second discrepancy between the $L_1L_{2,3}V$ data for the (100) surface and the theory, we believe that the reason that the theoretical *s*-like peaks are too large is that the approximations used to calculate the atomic matrix elements for $L_1L_{2,3}M_1$ transitions result in a considerable overestimate of their magnitudes. Evidence supporting this belief may be found in comparison of theory and experiment for the Auger spectrum of gas phase Ar.[19,20] In that case, as here, the $L_1L_{2,3}M_1$ matrix elements are considerably larger relative to the $L_1L_{2,3}M_{2,3}$ matrix elements than they should be to explain the data.[19]

In Fig. 8 we show the comparison of theory and experiment for the $L_1L_{2,3}V$ data from Si(100) when the calculated atomic matrix element

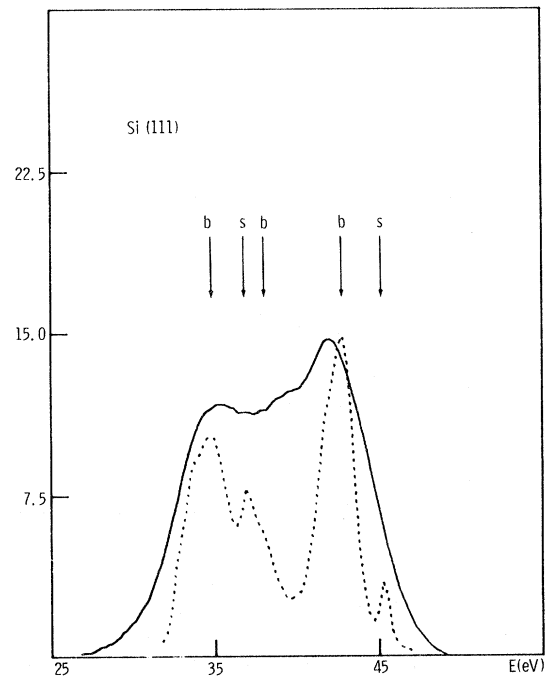

FIG. 9. Same as Fig. 8 for the (111) surface and with a shift upward in the theory curve of 3.2 eV.

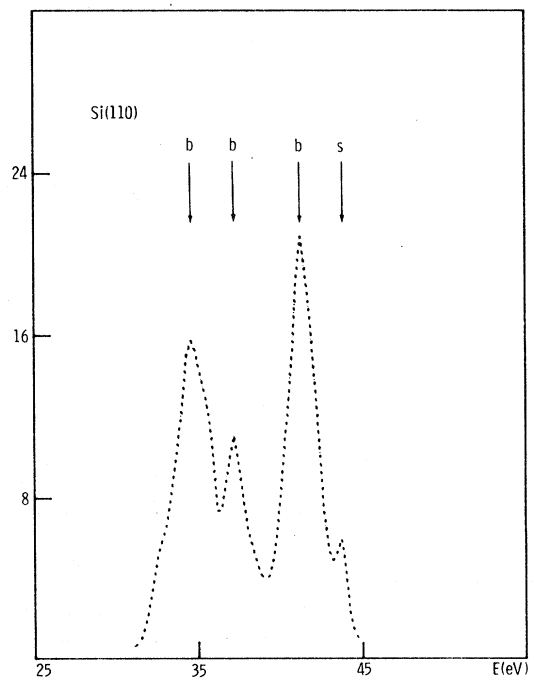

FIG. 10. Same as the theory curve of Fig. 8 for the (110) surface.

$R_0(0,1,1,0)$ is reduced by a factor $\frac{1}{2.5}$. Note that the agreement between theory and experiment is considerably improved in comparison to that in Fig. 7. Improved calculations of the $L_1L_{2,3}M_1$ matrix elements are therefore being undertaken,[21] with the hope of explaining this factor of $\frac{1}{2.5}$. In Figs. 9 and 10 for the Si (111) and (110) surfaces we have included this factor at the outset.

Let us turn finally to the comparison of theory and experiment for the $L_1L_{2,3}V$ line on the (111) surface, shown in Fig. 9. Here we note again a rough agreement in position of the three features in the data with the "bulk" features in the theory. However, again the dangling-bond peak of the theory is absent in the data. And additionally, the experimental curve seems too broad compared to the theoretical. Again, it may be that the high energy feature in the data includes contributions from both the leading bulk peak and the dangling bond (which might explain its breadth). Or it may be that on the reconstructed (111) surface there is no dangling-bond peak. For the (111) surface this latter hypothesis contradicts photoemission data[16] in which a dangling-bond peak has been reported.

The feature of the (111) data which is harder to explain is why the line extends to an energy several volts lower than the theoretical prediction. Again, this result may be a consequence of surface reconstruction, which could pull a back-bonding peak out of the bottom of the Si valence band. But it may also be a consequence of a many-electron effect such as the excitation of electron-hole pairs at the same time as the Auger decay occurs.

V. SUMMARY AND CONCLUSIONS

We have shown that the independent electron picture explains the discrepancy between the DOS model and experiment for the $L_{2,3}VV$ Auger lines of the Si (100) and (111) surfaces. For the $L_1L_{2,3}V$ transitions one-electron theory and experiment are not in very good agreement. Part of the problem, we believe, stems from the difficulty of calculating accurate atomic Auger matrix elements for low-energy transitions.[19,20] However, it also appears that to explain the discrepancy between $L_1L_{2,3}V$ data and theory, either improved surface models must be found, that show little structure due to surface states, or else many-electron effects must be invoked which smear the surface state peaks out of existence.

ACKNOWLEDGMENTS

We wish to thank J. E. Houston and M. G. Lagally for many useful discussions.

APPENDIX A

In this Appendix we present the results of evaluating the angular matrix element $A_{l_f,m_f;l_i,L_1,L_2}(\kappa)$ of Eq. (3.5). In terms of 3-j symbols this matrix element may be written in the form

$$A_{l_f,m_f;l_i,m_i;l_1,m_i,l_2m_{l_2}}(\kappa) = 4\pi[(2l_i+1)(2l_f+1)(2l_1+1)(2l_2+1)]^{1/2} \times (-1)^{m_f+m_{l_1}} \begin{pmatrix} l_i & \kappa & l_1 \\ 0 & 0 & 0 \end{pmatrix} \begin{pmatrix} l_f & \kappa & l_2 \\ 0 & 0 & 0 \end{pmatrix} \times \sum_{\beta=-\kappa}^{\kappa} \begin{pmatrix} l_i & \kappa & l_1 \\ m_i & \beta & -m_{l_1} \end{pmatrix} \begin{pmatrix} l_2 & \kappa & l_f \\ m_{l_2} & \beta & -m_f \end{pmatrix}, \quad \text{(A1)}$$

TABLE IV. Results for $l_i = 0$.

l_1	l_2	$A/4\pi$
0	0	$O(0,0)P(0,0)Q(0,0)$
0	1	$-O(0,1)\delta_{m_f,m_{l_2}}$
1	0	$-\frac{1}{3}O(1,1)\delta_{m_f,m_{l_1}}$
1	1	$\frac{1}{3}O(1,0)(-1)^{m_{l_1}}\delta_{m_{l_1},-m_{l_2}} + (\frac{2}{3})O(1,2)\times\{P(0,1)$ $\times[Q(2,1)/\sqrt{5} + Q(1,0)/\sqrt{10} + Q(0,-1)/\sqrt{30}]$ $+ P(0,0)[Q(1,1)/\sqrt{10} + Q(-1,-1)/\sqrt{10} + 2Q(0,0)/\sqrt{30}]$ $+ P(0,-1)[Q(-2,-1)/\sqrt{5} + Q(-1,0)/\sqrt{10} + Q(0,1)/\sqrt{30}]\}$

TABLE V. Results for $l_i = 1$.

l_1	l_2	$A/4\pi$
0	0	$-O(1,1)/3(-1)^{m_i}\delta_{m_i,-m_f}$
0	1	$O(1,0)/3\delta_{m_i,m_{l_2}} + (\sqrt{\frac{2}{3}})O(1,2)\{-P(1,0)[Q(0,1)/\sqrt{30}$ $+ Q(-1,0)/\sqrt{10} + Q(-2,-1)/\sqrt{5}\,] + P(0,0)[Q(1,1)/\sqrt{10} + \sqrt{\frac{2}{15}}$ $Q(0,0) + Q(-1,-1)/\sqrt{10}\,] - P(-1,0)[Q(0,-1)/\sqrt{30} + Q(1,0)/\sqrt{10}$ $+ Q(2,1)/\sqrt{5}\,]\}$
1	0	$O(0,0)\delta_{m_i,m_{l_1}} + \frac{1}{5}(\sqrt{6})O(2,2)\{-Q(2,0)P(-1,1)/\sqrt{5}$ $+ Q(1,0)/(\sqrt{10})[P(0,1) - P(-1,0)] + Q(0,0)/(\sqrt{30})[2P(0,0) - P(1,1)$ $- P(-1,-1)] + Q(-1,0)/(\sqrt{10})[P(0,-1) - P(1,0)] - Q(-2,0)/(\sqrt{5})P(1,-1)\}$
1	1	$-O(0,1)\delta_{m_f,m_{l_2}}\delta_{m_i,m_{l_1}} - \frac{6}{5}O(2,1)[-Q(1,1)/30B_3 - Q(1,0)/10B_4$ $+ Q(1,-1)/5B_5 + Q(0,1)/10B_2 + Q(0,0)/15B_3 + Q(0,-1)/10B_4$ $- Q(-1,-1)/30B_3 - Q(-1,0)/10B_2 + Q(-1,1)/5B_1]$ $+ (\frac{3}{5})(\sqrt{6})O(2,3)[Q(3,1)/(\sqrt{35})B_5 + Q(2,0)/(\sqrt{105})B_5$ $+ Q(2,1)/(\sqrt{105})B_4 - Q(1,1)/(5\sqrt{21})B_3 + 2/(5\sqrt{21})Q(1,0)B_4$ $+ Q(1,-1)/(5\sqrt{21})B_5 + Q(0,1)/(5\sqrt{14})B_2 - Q(0,0)/(5\sqrt{14})B_3$ $+ Q(0,-1)/(5\sqrt{14})B_4 - Q(-1,-1)/(5\sqrt{21})B_3 + 2/(5\sqrt{21})Q(-1,0)B_2$ $+ Q(-1,1)/(5\sqrt{21})B_1 + Q(-2,0)/(\sqrt{105})B_1 + Q(-2,-1)/(\sqrt{105})B_2$ $+ Q(-3,-1)/(\sqrt{35})B_1]$

which can be straightforwardly calculated. In Tables IV and V we present results for $l_i = 0$ and 1, respectively, and l_1 and $l_2 = 0$ and/or 1. Values for l_1 or $l_2 = 2$ are available from one of the authors.[22] As these other tables are lengthy, and not relevant to Si, we do not include them here.

We use the following notations in the tables:

$$O(a,b) \equiv \delta_{\kappa,a}\delta_{l_f,b}, \tag{A2}$$

$$P(a,b) \equiv \delta_{m_{l_i},a}\delta_{m_{l_1},b}, \tag{A3}$$

$$Q(a,b) \equiv \delta_{m_f,a}\delta_{m_{l_2},b}, \tag{A4}$$

$$B_1 \equiv P(1,-1), \quad B_2 = P(1,0) - P(0,-1),$$
$$B_3 \equiv 2P(0,0) - P(1,1) - P(-1,-1), \tag{A5}$$
$$B_4 \equiv P(-1,0) - P(0,1); \quad B_5 = P(-1,1).$$

*Research prepared for the U. S. Energy Research and Development Administration under Contract No. AT(29-1)-789.

[1]See, e.g., C. J. Powell, Phys. Rev. Lett. 30, 1179 (1973); J. E. Houston, J. Vac. Sci. Technol. 12, 255 (1974); L. I. Yin, I. Adler, T. Tsang, M. H. Chen, D. A. Ringers, and B. Crasemann, Phys. Rev. A 9, 1070 (1974).

[2]J. E. Houston, M. G. Lagally, and G. Moore (unpublished).

[3]For any crystal surface we define the WSFDOS to be the sum on j of the self-fold of the local DOS for the jth crystal layer times the factor $f_j \equiv \int_0^1 dv \exp(-2Z_j/\lambda v)$, where Z_j is the depth of the jth layer and λ is the inelastic mean free path. The form of f_j is chosen to account approximately for the number of electrons which can escape from depth Z_j, including the effect of increased path length for off-normal exit.

[4]A brief account of some of this work has already been published. See P. J. Feibelman, E. J. McGuire, and K. C. Pandey, Phys. Rev. Lett. 36, 1154 (1976).

[5]This factor of $\frac{1}{2}$ was inadvertently dropped in Eq. (3) of Ref. 4. As a consequence, the units for the "full theory" curve of Fig. 1 of that reference should be $2\pi \times 10^{-4}\hbar^{-1}$ rather than $4\pi \times 10^{-4}\hbar^{-1}$.

[6]J. A. D. Matthew and Y. Komninos, Surf. Sci. 73, 716 (1975).

[7]The fact that $\psi^*_{\vec{k}_{\parallel},E+V_0}$ should satisfy *incoming* boundary conditions has been widely discussed. See, e.g., G. Breit and H. A. Bethe, Phys. Rev. 93, 888 (1954).

[8]If we had used outgoing-wave boundary conditions (incorrectly), we would have $\exp\{-i[\delta_l + \frac{1}{2}\pi l - \arg\Gamma(l+1 + iZ/p_f a_0)]\}$ in Eq. (2.20) instead of the exponential that appears there.

[9]K. C. Pandey and J. C. Phillips, Phys. Rev. B 13, 750 (1976); Phys. Rev. Lett. 32, 1433 (1974).

[10]J. A. Appelbaum and D. R. Hamann, Phys. Rev. Lett. 31, 106 (1973).
[11]F. Herman and S. Skillman, *Atomic Structure Calculations* (Prentice-Hall, Englewood Cliffs, N.J., 1963). The method used to evaluate the matrix elements is described by E. J. McGuire, Phys. Rev. A 3, 587 (1971).
[12]Here $\mathcal{R}$ is the Rydberg and a_0 the Bohr radius.
[13]The positions of the experimental lines are, in fact, unknown to the extent that the work function for each Si surface differs from that of the stainless-steel anodes used in Ref. 2 to detect the Auger electrons. Thus it is not clear what our small shifts in E_c may mean. J. E. Houston (private communication).
[14]J. A. Appelbaum and D. R. Hamann, Phys. Rev. B 12, 5590 (1975).
[15]J. A. Appelbaum and D. R. Hamann, Phys. Rev. Lett. 35, 729 (1975).
[16]J. E. Rowe and H. Ibach, Phys. Rev. Lett. 32, 423 (1974).
[17]W. A. Harrison, Surf. Sci. 55, 1 (1976); M. B. Webb, T. D. Poppendieck, T. C. Ngoc, and T. Tommet, Bull. Am. Phys. Soc. (to be published).
[18]This lifetime is mainly due to the very Coster-Kronig transition we are considering.
[19]W. Mehlhorn, Z. Phys. 208, 1 (1968).
[20]E. J. McGuire, Phys. Rev. A 11, 1880 (1975).
[21]H. P. Kelly (private communication).
[22]E. J. McGuire, Sandia Laboratories Report No. SAND76-0374, Albuquerque, New Mexico (unpublished).